Research in Astronomy and Astrophysics, 24:115009 (9pp), 2024 November https://doi.org/10.1088/1674-4527/ad849a

Deep Neural Network Closed-loop with Raw Data for Optical Resident Space Object Detection

He Zhao[1,2], Rong-Yu Sun[1], and Sheng-Xian Yu[1]
[1] Purple Mountain Observatory, Chinese Academy of Sciences, Nanjing 210023, China; rysun@pmo.ac.cn
[2] School of Astronomy and Space Science, University of Science and Technology of China, Hefei 230026, China
Received 2024 June 13; revised 2024 August 25; accepted 2024 October 5; published 2024 November 4

Abstract

Optical survey is an important means for observing resident space objects and space situational awareness. With the application of astronomical techniques and reduction method, wide field of view telescopes have made significant contributions in discovering and identifying resident space objects. However, with the development of modern optical and electronic technology, the detection limit of instruments and infrastructure has been greatly extended, leading to an extensive number of raw images and many more sources in these images. Challenges arise when reducing these data in terms of traditional measurement and calibration. Based on the amount of data, it is particularly feasible and reliable to apply machine learning algorithms. Here an end-to-end deep learning framework is developed, it is trained with a priori information on raw detections and the automatic detection task is performed on the new data acquired. The closed-loop is evaluated based on consecutive CCD images obtained with a dedicated space debris survey telescope. It is demonstrated that our framework can achieve high performance compared with the traditional method, and with data fusion, the efficiency of the system can be improved without changing hardware or deploying new devices. The technique deserves a wider application in many fields of observational astronomy.

Key words: methods: data analysis – techniques: image processing – surveys

1. Introduction

The development of satellite and launch technology has led to a significant number of resident space objects (RSOs) in orbit, e.g., communication and navigation satellites, rocket bodies and space debris produced consequently, which pose a threat to the safety and sustainability of the space environment. Obtaining effective information on RSOs, including their positions and status, which is also referred to as space situational awareness (SSA), is essential and crucial. Optical survey utilizing astronomical telescope is an important passive means for observing and detecting RSOs (Schildknecht 2007), and compared with other active ways, like laser ranging (Zhang et al. 2012) and radar (Tingay et al. 2013), it is more appropriate to perform surveys for high-Earth orbital regions (Matney et al. 2004; Sun et al. 2015). Furthermore, considering the relatively low economic cost of optical infrastructures, it is feasible to develop telescope arrays (Zhang & Zhao 2021) or make a network with multiple sites (Molotov et al. 2008).

Wide field of view telescopes are widely used in optical RSO surveys, and because large-scale sky fields can be surveyed in a shorter time, the efficiency is promoted. The consequent object detection and extraction algorithms have also been developed and deployed, among which the traditional astronomical source extraction techniques, including SExtractor (Bertin & Arnouts 1996) and DAOPHOT (Stetson 1987; Schechter et al. 1993), are widely applied and have played important roles. Meanwhile, dedicated algorithms are also proposed in specific applications and achieve great performance in object detection. In detail, considering the relative movement between background stars and RSOs, the images of stars and RSOs appear as different shapes, according to different observing strategies, and techniques utilizing masking or streak detection work effectively in data reduction (Kouprianov 2008; Sun et al. 2016; Hickson 2018). Based on the movement characteristics of RSOs, methods are also proposed to extract and correlate objects from consecutive frames in celestial coordinates (Sun et al. 2019; Du et al. 2022; Zhang et al. 2024). Furthermore, image processing methods including morphology transformation (Sun & Zhao 2013) and restoration (Sun & Jia 2017) as well as image stacking (Yanagisawa et al. 2005) are widely used to improve the signal-to-noise ratio (SNR) of object and promote the detection efficiency.

However, with the development of telescope and sensor technology, the detection limit of infrastructures nowadays is greatly extended, leading to an extensive number of raw images and many more sources in images. For example, the number of sources in one wide field image can reach up to greater than 10,000, and due to the deployment of sensors with fast readout speed, the frame rate is increased significantly and extensive amounts of data are acquired. Challenges arise for previous

data reduction and object detection methods, the extraction efficiency and time cost are affected, and the performance is limited.

The development of artificial intelligence has triggered a technological revolution, leading to various object detection models that, after training, are capable of extracting different types of sources from a single frame, akin to human perception. This kind of technique requires large amounts of data to train the parameters of the model for specific tasks. Considering the big data obtained by modern astronomical infrastructures, it is particularly feasible to apply these techniques.

Significant breakthroughs have been made in these areas. For the Sloan Digital Sky Survey (SDSS), the You Only Look Once (YOLOv4) is adopted to develop the source detection and classification network (He et al. 2021). A modified YOLOv3 is presented for redshift galaxy cluster detection and similar performance compared with the traditional method is achieved (Grishin et al. 2023). The convolutional neural network (CNN) is also widely applied in data reduction of wide field telescopes (Jia et al. 2020), e.g., detecting images with asteroid streaks (Wang et al. 2022a) and finding blue horizontal-branch stars (He et al. 2023). In addition to these one-stage methods, two-stage-based models are also used for point and streak source detection in dedicated applications (Dumitrescu et al. 2022). However, it should be noted that in these applications the models are trained and validated mostly on simulated data, and considering the lack of raw training data, the performance is limited and it deserves to be further investigated.

In our work, a deep learning neural network based on the YOLOv5 model is developed to detect and extract RSOs from large amounts of raw CCD images. Our method is trained on raw data with a priori information obtained in traditional ways, and based on the morphological difference between stars and RSOs, the model learns these features and extracts RSO images from a single frame with their measurement information. The performance is evaluated also on raw data. It is demonstrated that high efficiency is achieved using our closed-loop network, and with data fusion, the promotion of the system can be obtained. In Section 2 the principle and algorithm are introduced, the application is described in Section 3 and the results are discussed in Section 4. In Section 5 the conclusion is drawn.

2. Principles and Algorithms

The deep learning process includes two key steps: data set construction and neural network structure. In this era of big data, high-quality data play a crucial role in deep learning, and most data sets are constructed by manual labeling and annotation. On the other hand, an appropriate structure would exhibit excellent performance for specific tasks. For the data set, we propose an automatic labeling method, which utilizes previously applied object detection and identification algorithms, extracting the position of RSO images in real-time and based on this information the data set for model training is built. This approach saves an extensive amount of time and generates a comprehensive data set. Our method also optimizes label parameters based on distributions and experiments. Furthermore, we employ image transformations with a priori knowledge to promote object detection and improve efficiency, especially for faint cases. For the network architecture, considering the RSO images appear as small-scale and faint sources in a large field of view frame, the network structure is adjusted in the neck and head areas to better detect objects of specific categories.

2.1. Network Architecture

YOLO is one kind of cutting-edge convolutional neural network (CNN), which provides real-time object detection ability. Different from two-stage CNN detection networks, which utilize two separate networks firstly to detect candidates and then classify them, YOLO employs a single network for positioning with classification to achieve end-to-end detection, fulfilling our requirements well. During reduction, it divides input data into several grid cells and predicts bounding boxes in each grid. These bounding boxes are presented in the format (x, y, w, h, C, $p(c_1)$, $p(c_2)$,...), where (x, y) is the center coordinates of an object, and (w, h) represents the object size including the width and height. C is the confidence coefficient for a detection and ($p(c_1)$, $p(c_2)$,...) show the probabilities for different classes respectively. A specific loss function is given to evaluate the differences between the prediction and ground truth of the bounding boxes. By optimizing parameters in the neural network through taking the derivative backwards to reduce the loss function value, the model learns the features of our data set gradually. The loss function for our network is given as follows.

$$\mathrm{Loss_{total}} = \alpha * \mathrm{Loss_{BOX}} + \beta * \mathrm{Loss_{OBJ}} + \gamma * \mathrm{Loss_{CLA}}, \tag{1}$$

where α, β and γ are the weighting coefficients. $\mathrm{Loss_{BOX}}$ is the difference in location between the prediction and ground truth. For YOLOv5, Complete Intersection over Union (CIOU) is used to obtain this distance.

$$\mathrm{Loss_{BOX}} = L_{\mathrm{CIOU}}(\rho, c, v) = 1 - \mathrm{IOU} + \frac{\rho^2}{c^2} + \frac{v^2}{(1 - \mathrm{IOU}) + v}, \tag{2}$$

where Intersection over Union (IOU) is calculated as follows.

$$\mathrm{IOU} = \frac{\mathrm{Intersection}}{\mathrm{union}}. \tag{3}$$

The Intersection for a given bounding box can be derived as below.

$$\begin{aligned}\text{Intersection} = &\left\{\min\left(x+\frac{w}{2}, x^{gt}+\frac{w^{gt}}{2}\right)\right.\\ &\left.-\max\left(x-\frac{w}{2}, x^{gt}-\frac{w^{gt}}{2}\right)\right\}\\ &*\left\{\min\left(y+\frac{h}{2}, y^{gt}+\frac{h^{gt}}{2}\right)\right.\\ &\left.-\max\left(y-\frac{h}{2}, y^{gt}-\frac{h^{gt}}{2}\right)\right\},\end{aligned} \tag{4}$$

where label gt means the parameter is given by ground truth, and the symbols without gt are obtained by prediction. Then Union is obtained.

$$\text{Union} = w*h + w^{gt}*h^{gt} - \text{Intersection}, \tag{5}$$

here v, ρ and c are introduced to represent the distance more accurately.

$$v = \frac{4}{\pi^2}(\arctan\frac{w^{gt}}{h^{gt}} - \arctan\frac{w}{h}), \tag{6}$$

$$\rho^2 = (x-x^{gt})^2 + (y-y^{gt})^2, \tag{7}$$

$$\begin{aligned}c^2 = &\left(\max\left(x+\frac{w}{2}, x^{gt}+\frac{w^{gt}}{2}\right) - \min\left(x-\frac{w}{2}, x^{gt}-\frac{w^{gt}}{2}\right)\right)^2\\ &+\left(\max\left(y+\frac{h}{2}, y^{gt}+\frac{h^{gt}}{2}\right) - \min\left(y-\frac{h}{2}, y^{gt}-\frac{h^{gt}}{2}\right)\right)^2.\end{aligned} \tag{8}$$

Loss_{OBJ} refers to the reliability of the predicted rectangle compared with the actual ground truth box, and Loss_{CLA} denotes the difference between the predicted class and a specific class. The YOLOv5 model employs Binary Cross Entropy (BCE) loss to evaluate this variance.

$$\text{Loss}_{\text{CLA}} = -\frac{1}{n}\sum_{i=1}^{n} y_i \log p(i) - (1-y_i)\log(1-p(i)), \tag{9}$$

where n represents the number of pixels within the predicted rectangle. The binary label y_i indicates either false or true, with a value of 0 or 1 respectively. The probability $p(i)$ denotes the likelihood predicted by the model that a given pixel belongs to the specified region or class.

2.2. Network Optimization

Different from a multiple-class detection task, for our network the model is only trained with a single object class. Consequently, in the loss function, β is set to zero for simplicity. On the other hand, considering that the sizes of RSO images are generally small relative to the whole frame and the distribution of images is similar to a classic Gaussian function, we modify Loss_{BOX} with the Normalized Wasserstein Distance (NWD; Wang et al. 2022b). The new Loss_{BOX} is expressed as follows.

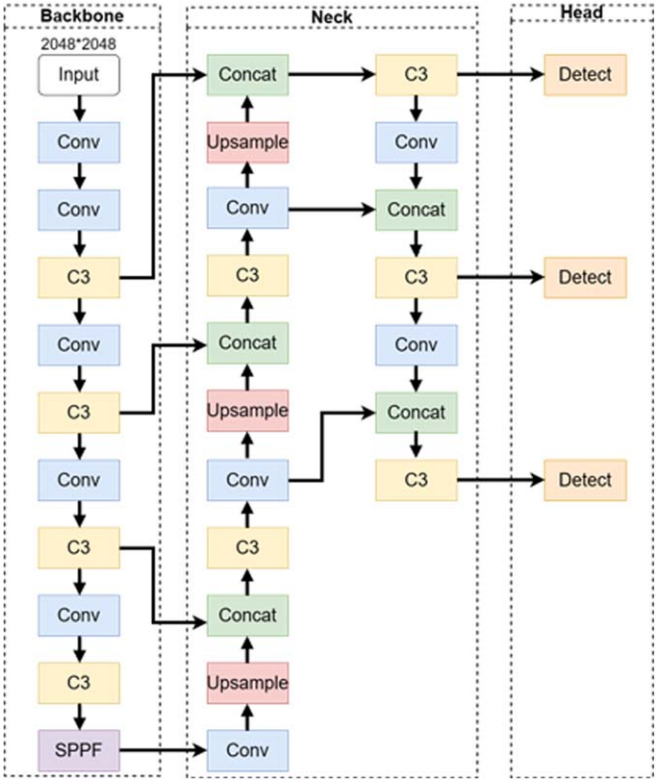

Figure 1. The architecture of our network.

$$\begin{aligned}&W_2^2(x, y, w, h, x^{gt}, y^{gt}, w^{gt}, h^{gt})\\ &= \left\| \left[x, y, \frac{w}{2}, \frac{h}{2}\right]^2, \left[x^{gt}, y^{gt}, \frac{w^{gt}}{2}, \frac{h^{gt}}{2}\right]^2 \right\|_2^2,\end{aligned} \tag{10}$$

$$\text{NWD}(x, y, w, h, x^{gt}, y^{gt}, w^{gt}, h^{gt}) = \exp\left(-\frac{\sqrt{W_2^2}}{C}\right), \tag{11}$$

$$\text{Loss}_{\text{BOX}} = \text{Loss}_{\text{NWD}} = 1 - \text{NWD}. \tag{12}$$

The parameter C is determined due to the data set and is set to 16 to optimally perform the training task.

For the neck structure, we employ an additional upsample layer for detecting faint and small RSO images. Different from the fundamental $P3$, $P4$ and $P5$ layers, we substitute $P5$ with $P2$ in the detection header, which results in a 40% reduction in model parameters and improves detection capability. The modified structure is illustrated in Figure 1.

3. Application

3.1. Observations

A dedicated telescope for RSO survey is utilized to perform trial observation and, based on the raw data, the efficiency of

Table 1
Detailed Information on the Telescope and CCD Frame

Parameter	Value
Aperture	500 mm
Field of view	$2.^{\circ}2 \times 2.^{\circ}2$
Frame size	2048×2048
Pixel scale	$3.''9$
Dynamic range	$0 \sim 65535$
CCD operating mode	Frame transfer

our network is analyzed. Detailed information on this telescope is shown in Table 1.

During observation, considering the dynamical characteristics of high-Earth orbital RSOs, their angular movement is slow relative to a ground observer, hence the stare mode is adopted. This means the telescope keeps pointing to a specific horizon field during exposure while the drive is turned off. The exposure time for a single frame is 2 s, and consecutive images are acquired with the same azimuth and elevation. With this strategy, the background stars appear as short streaks in images while RSOs located in the high-Earth orbital region appear as points. Due to the relatively wide field, several RSOs may appear in the same image, as shown in Figure 2.

The time interval for switching fields is 2 minutes, and approximately 15 raw CCD frames can be obtained for each field, considering the readout time of the CCD camera and the pointing setting of the telescope. The observations are performed in 4 nights. After the large amounts of raw CCD images are acquired, object detection and tracklet extraction are performed with previous algorithms. Here tracklet refers to a series of measured information of the same object, including centroids and observed positions in right ascension and declination. In detail, the sources in each image are extracted and their measurement positions are obtained, then with astrometry their equatorial positions are derived. According to the movement difference between stars and RSOs in consecutive images, the RSO candidates are detected and the tracklets are generated. At last, these tracklets are correlated with the catalog (Yu et al. 2021); the ones not correlated to the catalog are recognized as false detections and the ones correlated with the catalog are taken as a priori information, which is used in model training and validation. After optimization, our previous reduction pipeline can detect the RSOs in near real-time. It should be noted that after the tracklets are extracted with the network we developed, the orbit correlation is also performed and the number of false detections and correlated objects is obtained, then the performance of our network is evaluated.

Detailed results obtained with the previous method are shown in Table 2, including the fields observed, the number of raw images acquired each day, the number of extracted tracklets, and uncorrelated and correlated objects after reduction. The distribution of eccentricity and semimajor axis of correlated RSOs is shown in Figure 3. It can be found that approximately 9000 raw images can be obtained each day, and more than 2800 tracklets can be extracted. It should be noted that generally one tracklet may include $8 \sim 15$ position measurements, hence the extensive amounts of a priori detections are feasible and reliable for the application of a CNN.

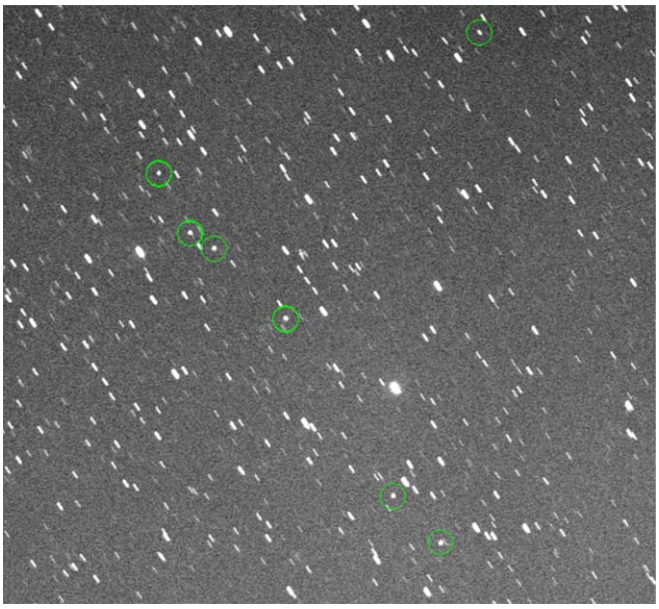

Figure 2. Snapshot of a part of the raw CCD image, the green circles indicate six RSOs in the image.

Table 2
The Results of the Observations with Previous Methods

Day	Observed Fields	Images	Extracted Tracklets	False Detections	Correlated Objects
1	695	9032	2816	214	537
2	693	9057	2903	214	584
3	693	8969	2867	418	556
4	691	8739	2835	147	582

3.2. Dataset Construction

The obtained data set provides information about RSOs, including their position measurements and image sizes. Artificial intelligence models can be applied to learn features from the data set and then perform object detection on new data. Therefore, it is crucial to construct a high-quality data set. Generally, the measured position (x, y) and dimensions (width,

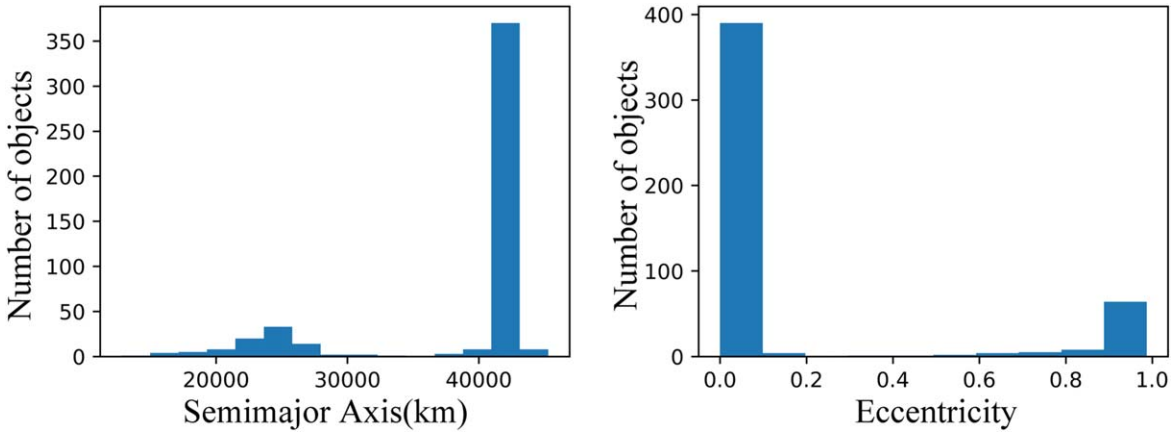

Figure 3. The distribution of eccentricity and semimajor axis of correlated RSOs.

height, w, h) require manual annotation. In our test based on previous object detection methods, we have already obtained the measured positions of RSOs. Then another issue is choosing the optimal box size for the data set. The width and height of all RSO images are obtained with SExtractor using a 3σ threshold, and the distribution is shown in Figure 4. It indicates that the majority of RSO images (approximately 85%) are smaller than 20×20 pixels, and they are different from the background stars, which exhibit high pixel values and larger sizes. Considering the size of the whole image is 2048×2048, these are typically small and faint objects. According to the distribution and after some investigations, the width and height are both set as 16 pixels to achieve a balance between performance and efficiency in model training.

The variations of background levels and object brightness potentially cause confusions within the model, and data normalization is crucial. To address this challenge, a gray transformation is applied to augment the signals of faint RSO images. The transformation is performed as follows.

$$y \equiv \begin{cases} 0 & x \leqslant bkg \\ \dfrac{x - bkg}{5\sigma} & bkg < x \leqslant bkg + 5\sigma, \\ 1 & bkg + 5\sigma < x \end{cases} \tag{13}$$

where bkg and σ are mean background level and standard deviation obtained by SExtractor respectively. The effect of the augment is shown in Figure 5.

3.3. Model Training

Although the model parameters have been optimized, the YOLO network still has more than six million parameters. The training process refers to adjusting these parameters to task-specific characteristics. Starting from all zero or random values would cost much more epochs for these model parameters to converge, and it consumes a lot more time on a large data set. Parameter initialization can promote the process and reduce the time spent on training epochs, so instead of training the entire data set, we make a smaller data set at first, and it is used for

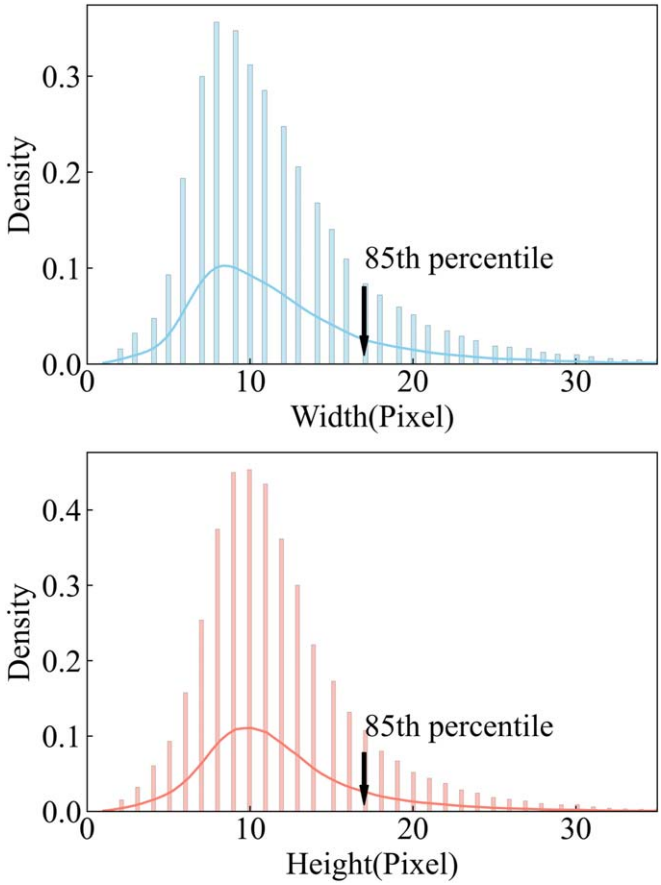

Figure 4. The width and height distribution for all RSO images.

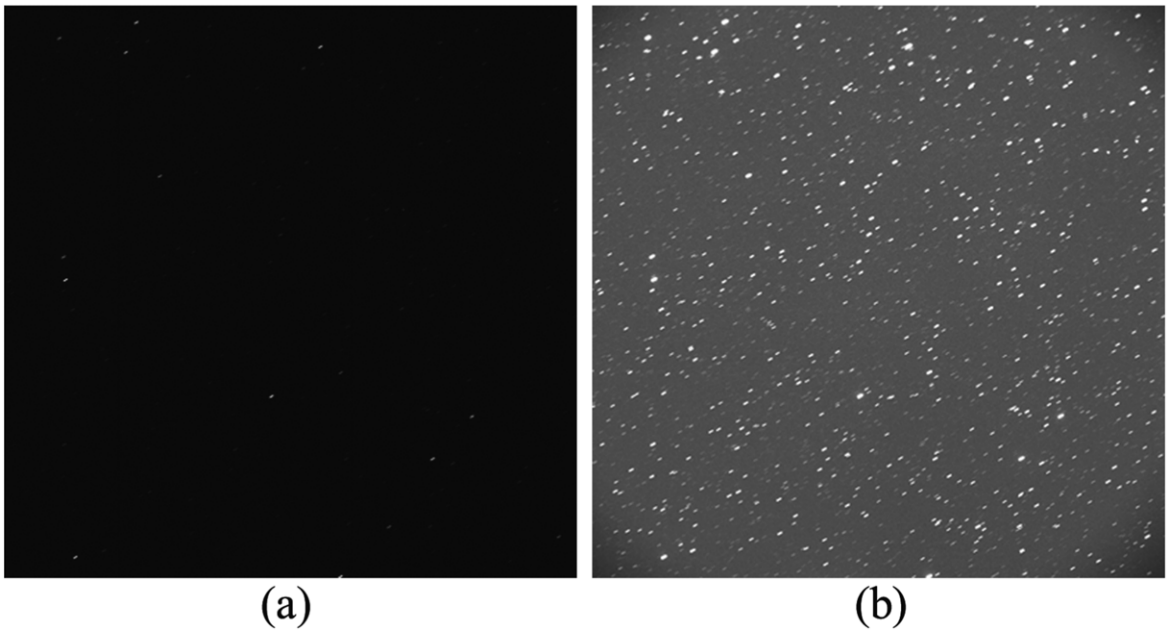

Figure 5. The gray transformation for an image. Left: before transformation. Right: after transformation.

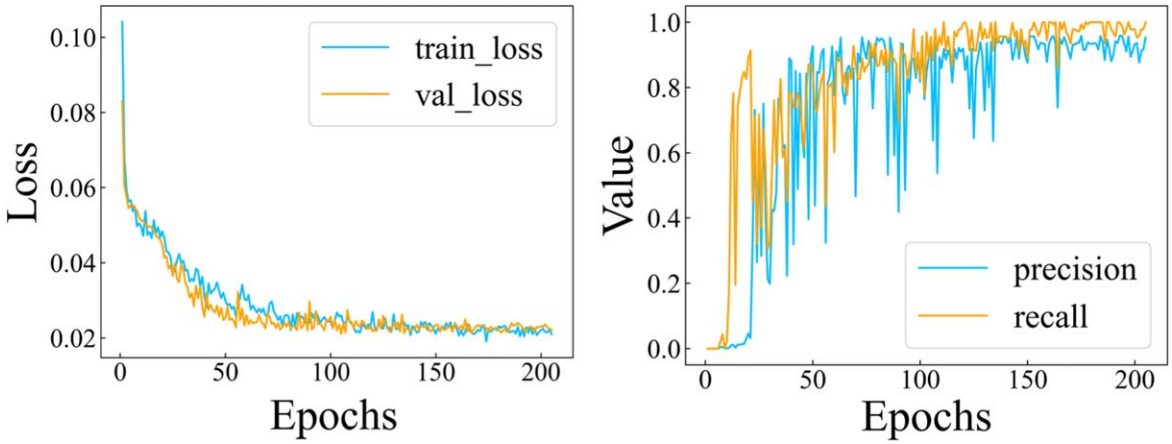

Figure 6. The performance of initial weight training.

pre-training to obtain initial weights in our RSO detection task. This data set is constructed with 200 randomly selected images, based on the RSO images from the first day and with a 3: 1 ratio of training to validation sets. It should be noted that all these images are manually labeled to avoid abnormal conditions like the presence of streaks or dense star fields. It costs approximately 1 hr to perform the pre-training and the initial weights are obtained for subsequent model training. With the pre-trained weights, for a training set with one-day of data, the model converges in approximately 50 epochs and the time cost is approximately 10 hr instead of 40 hr with a personal desktop with an NVIDIA RTX 3060 (6G). It should be noted that the time cost would be reduced to approximately 2 hr if a professional workstation with more GPUs is utilized. The loss function of the training and validation for the initial weight training is shown in Figure 6, along with the precision and recall curves. These indicate that the loss function decreased significantly and converged after 150 epochs, while the precision and recall rates approach 1 and achieve warm up for subsequent training.

To analyze the performance of our network, two different training and testing strategies are used for comparison. For the first strategy, we train the model with the data set from day 1 and test the model on the data set from day 2, then we train the

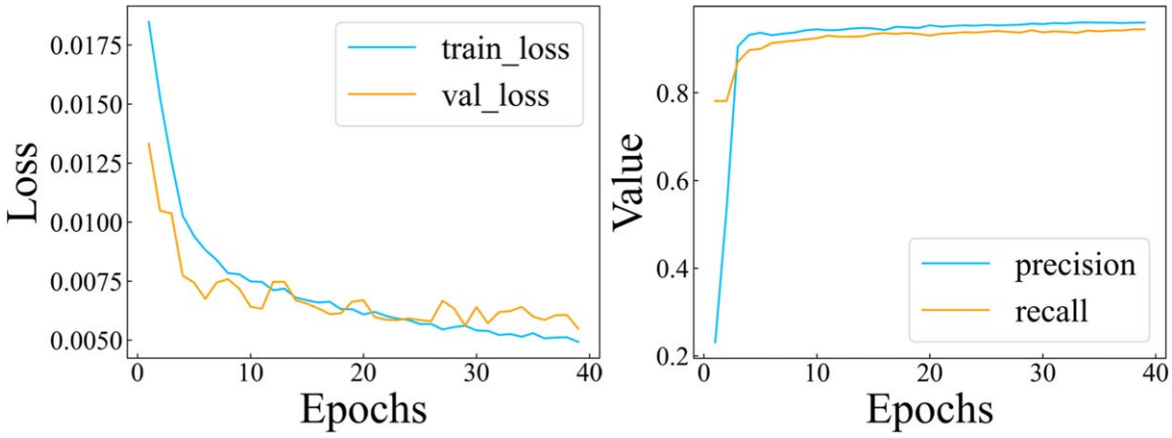

Figure 7. The performance of model training.

model based on the data set from day 3 and test the model with the data set from day 4. Each data set includes more than 7000 images and 35,000 labels, with a 3: 1 ratio of training to validation sets. When adopting the second strategy, the data from the first two days are used for training, and the data from the remaining two days are used for testing. The convergence epoch remains at 40 for both two strategies, but the training time for the second strategy increases due to the data size being doubled. It is demonstrated in Figure 7 that the pre-trained weights work effectively, and the training process starts from low loss and high recall rate so the time cost is saved.

4. Results and Discussions

After the network is trained, we evaluate its performance on the test set. We also analyze the new objects detected only by our network to investigate the improvements. In the object detection phase, after the object detection results are obtained for each frame, a breadth-first search strategy is used, which means measurement positions of all potential candidates are generated, regardless of their confidence levels. Then to minimize false alarms, we pick the first eight candidates based on their confidence ratio. Coupled with the well-trained model, the detection efficiency is promoted by this way.

With the two strategies mentioned previously, for each sky field the consecutive detection results are extracted, the tracklets are obtained and then the orbit correlation is performed. The results are shown in Tables 3 and 4 respectively. It can be found that both training strategies result in more correlated tracklets and detected objects than the traditional method, so their performances are better.

Furthermore, with the pre-trained weights, our network completes object detection in less than 0.1 s for a 2048×2048 frame, not accounting for the file I/O time cost. For comparison, the traditional method will cost $1 \sim 2$ s on the detection phase. It should be noted that this implementation benefits from the structure of CNNs. If the frame size increases dramatically which is likely to happen in the future, the time cost will not be extended significantly, but in contrast, for traditional image processing methods, the time cost will be multiplied accordingly.

Table 3
The Detection Result of First Application Strategy

Day	Objects	Extracted Tracklets	False Detections
1	535	2805	204
2	588	2939	91
3	564	2862	398
4	583	2841	136

Table 4
The Detection Result of Second Application Strategy

Day	Objects	Extracted Tracklets	False Detections
1	537	2804	193
2	590	2955	21
3	563	2874	422
4	585	2851	125

Further investigations are made based on the data obtained with the second strategy, which extracts more RSOs and tracklets, with fewer false detections. The magnitude distribution of detections obtained with the traditional way and the developed network on the second day is shown in Figure 8, which demonstrates the most detections and tracklets and the tail on the faint end is more even in terms of the magnitude distribution. It is demonstrated that the distributions are similar, with a peak between $10 \sim 12$ mag and the faintest detections

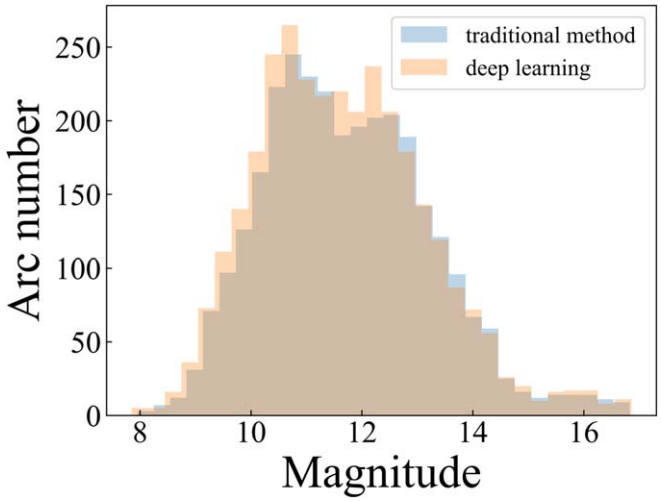

Figure 8. Magnitude distribution of detections with traditional method and our presented network.

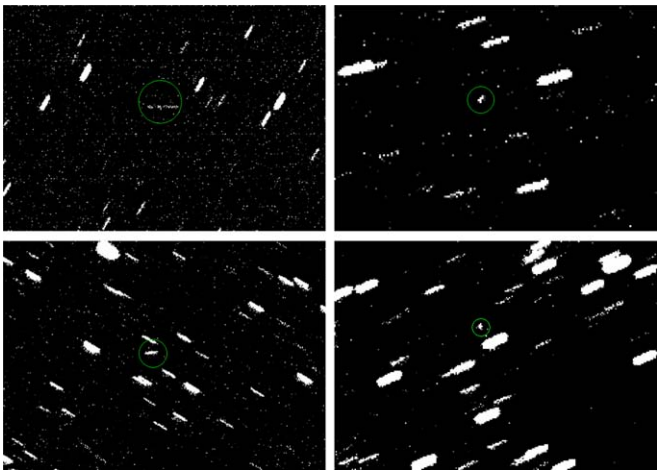

Figure 9. The images of four newly detected RSOs.

greater than 16 mag. Our method achieves a slightly better performance both for bright and faint objects. The details are shown in Table 5. It can be found that new RSOs are detected from the images from all four days. Certainly, some tracklets and objects are only detected by our network or the previous traditional way, hence the detections with these two methods are different. The images of newly detected objects are shown in Figure 9. These images indicate that these new detections are not just point-like, but also appear as streaks or other irregular shapes. After calculating their apparent angular velocity, it suggests that they are typical RSOs located in the high-Earth orbital region. The semimajor axis and eccentricity of these objects obtained with orbit determination are shown in Figure 10, and it is demonstrated that most of the newly

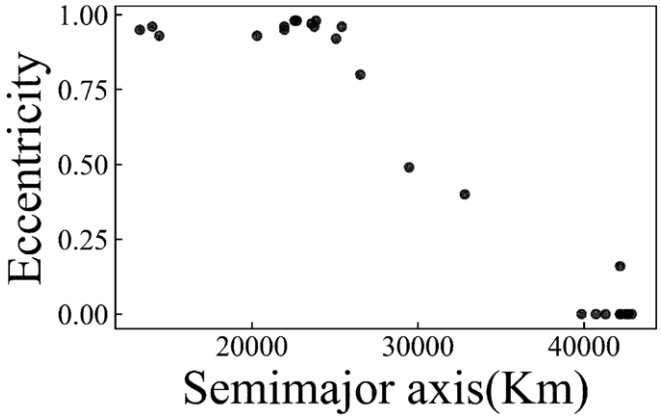

Figure 10. The semimajor axis and eccentricity of the newly detected objects.

Table 5
Newly Detected Objects Compared with Traditional Method

Day	New Objects	New Tracklets
1	13	75
2	29	414
3	13	48
4	13	83

detected objects are in highly elliptical orbits (HEOs), which exhibit unique dynamical characteristics. It should be noted that with data fusion, it is evident that the number of tracklets and objects will be improved without deploying new infrastructures, and the efficiency of the system is improved.

5. Conclusions

Due to the development of modern optical and electronic technologies, the infrastructure and instruments for the RSO survey have been greatly improved. Challenges arise in data reduction with these large amounts of data utilizing traditional ways. Here a novel object detection technique using deep learning is developed. Based on the end-to-end deep learning framework, the model is both trained and tested on large amounts of raw data. The results demonstrate that similar performance is achieved compared with previous methods, and the data can be reduced in real-time. In addition, our network detects a number of new tracklets and objects, improving the efficiency of the system. It is shown that with AI-based techniques strong synergy can be achieved for astronomical data reduction and it certainly will play vital roles in the future.

Acknowledgments

This work was funded by the National Natural Science Foundation of China (NSFC, grant Nos. 12473079 and

12073082), and the National Key R&D Program of China (No.2023YFF0725300). The authors would like to thank the anonymous reviewers and Editor in Chief for the valuable comments that helped to substantially improve the manuscript.

References

Bertin, E., & Arnouts, S. 1996, ApJS, 117, 393
Du, J., Hu, S., Chen, X., & Cao, H. 2022, MNRAS, 511, 3377
Dumitrescu, F., Ceachi, B., Truică, C.-O., et al. 2022, Aeros, 9, 520
Grishin, K., Mei, S., & Ilic, S. 2023, A&A, 677, A101
He, Y., Wu, J., Wang, W., Jiang, B., & Zhang, Y. 2023, PASJ, 75, 1311
He, Z., Qiu, B., Luo, A. L., et al. 2021, MNRAS, 508, 2039
Hickson, P. 2018, AdSpR, 62, 3078
Jia, P., Liu, Q., & Sun, Y. 2020, AJ, 159, 212
Kouprianov, V. 2008, AdSpR, 41, 1029
Matney, M. J., Stansbery, E., Africano, J., et al. 2004, AdSpR, 34, 1160
Molotov, I., Agapov, V., Titenko, V., et al. 2008, AdSpR, 41, 1022
Schechter, P. L., Mateo, M., & Saha, A. 1993, PASP, 105, 1342
Schildknecht, T. 2007, A&ARv, 14, 41
Stetson, P. B. 1987, PASP, 99, 191
Sun, R., & Jia, P. 2017, PASP, 129, 044502
Sun, R. Y., Yu, S. X., Zhao, C. Y., et al. 2019, PASJ, 71, 67
Sun, R. Y., Zhan, J. W., Zhao, C. Y., et al. 2015, AcAau, 110, 9
Sun, R. Y., & Zhao, C. Y. 2013, RAA, 13, 604
Sun, R. Y., Zhao, C. Y., & Lu, Y. 2016, RAA, 16, 29
Tingay, S. J., Kaplan, D. L., McKinley, B., et al. 2013, AJ, 146, 103
Wang, F., Ge, J., & Willis, K. 2022a, MNRAS, 516, 5785
Wang, J., Xu, C., Yang, W., & Yu, L. 2022b, arXiv:2110.13389
Yanagisawa, T., Nakajima, A., Kadota, K.-I., et al. 2005, PASJ, 57, 399
Yu, S. X., Wang, X., & Zhu, T. L. 2021, AdSpR, 68, 71
Zhang, B., Hu, S., Du, J., et al. 2024, PASP, 136, 054502
Zhang, C., & Zhao, C. Y. 2021, AnABC, 93, e20200827
Zhang, Z. P., Yang, F. M., Zhang, H. F., et al. 2012, RAA, 12, 212